J. Fluid Mech. (1999), *vol.* 378, *pp.* 269–289. Printed in the United Kingdom

A numerical investigation of resonant interactions in adverse-pressure-gradient boundary layers

By CHONGHUI LIU AND S. A. MASLOWE

Department of Mathematics, McGill University, Montreal, PQ H3A 2K6, Canada

(Received 26 August 1997 and in revised form 2 July 1998)

We present direct numerical simulations of the spatial development of normal mode perturbations to boundary layers with Falkner–Skan velocity profiles. Values of the pressure gradient parameter considered range from very small, i.e. nearly flat-plate conditions, to relatively large values corresponding to incipient separation. In almost all cases, we find that the most effective perturbation is one composed of a plane wave and a pair of oblique waves inclined at equal and opposite angles to the primary flow direction. The frequency of the oblique waves is half that of the fundamental plane wave and because the conditions for resonance are satisfied exactly, all modes share a common critical layer, thus facilitating a strong interaction.

The oblique waves initially undergo a parametric type of subharmonic resonance, but in accordance with recent analyses of non-equilibrium critical layers, the system subsequently becomes fully coupled. From that point on, the amplification of all modes, including the plane wave, substantially exceeds the predictions of linear stability theory. Good agreement is obtained with the experimental small pressure gradient results of Corke & Gruber (1996). Our growth rates are slightly larger owing to slight differences in initial conditions (e.g. the angle of inclination of the oblique waves).

The spectral element method was used to discretize the Navier–Stokes equations and the preconditioned conjugate gradient method was used to solve the resulting system of algebraic equations. At the inflow boundary, Orr–Sommerfeld modes were employed to provide the initial forcing, whereas the buffer domain technique was used at the outflow boundary to prevent convective wave reflection or upstream propagation of spurious information.

1. Introduction

In many engineering applications, the transition of boundary layers to turbulence occurs in a region of adverse pressure gradient. This is the case, for example, with air flow over wings that are moderately swept. Transition on such wings is most likely to take place in the adverse pressure gradient region past the maximum thickness point. Given the practical importance of pressure gradient flows and the fact that the basic instability mechanism is different from the Tollmien–Schlichting instabilities that occur in a flat-plate boundary layer, it is most surprising that the literature is so much more extensive for the Blasius case.

It is well known that shear flows with inflectional velocity profiles are linearly unstable on an inviscid basis and the effects of viscosity are generally stabilizing.

The Blasius boundary layer profile, on the other hand, owing to the absence of a vorticity maximum would be stable without viscosity. However, viscosity turns out to be destabilizing in the Blasius case as a result of the very subtle Tollmien–Schlichting mechanism. The growth rates associated with this mechanism are relatively small compared, for example, with the inflection point instability in a mixing layer. The contrast between these two flows serves, in fact, as a focal point in the chapter on shear flow stability in the monograph edited by Swinney & Gollub (1985).

From a fundamental point of view, the preceding considerations make it clear that the adverse pressure gradient boundary layer is a most interesting example for detailed study because it combines features of the two situations discussed above. When the pressure gradient is very small and the Reynolds number not too large, the instability can arguably be regarded as a modification of the Blasius case. On the other hand, for flows closer to separation and subject to stronger pressure gradients, the instability is inviscid in character and it is not clear to what extent any knowledge gained through the study of flat-plate boundary layers is applicable.

The foregoing discussion was centred on linear instability mechanisms, but similar issues arise from consideration of certain finite-amplitude analyses that have appeared recently. These include the closely related studies of Goldstein & Lee (1992), Wu (1992) and Mallier & Maslowe (1994). Although only the first of these dealt specifically with the adverse pressure gradient boundary layer, what turns out to be most important is that each treated resonant interactions in a shear flow with an inflectional velocity profile and utilized the same type of critical layer balance. The end result in each case was a pair of coupled integro-differential equations describing the amplitude evolution of the interacting disturbances. These equations exhibit explosive instabilities, i.e. singularities that are reached in a finite time (or distance). Of course, the stability literature abounds with such singular solutions and usually these merely indicate a breakdown of the theory as the disturbance amplitudes become large. Hence, one of the goals of the present research was to see if in a direct numerical simulation of the Navier–Stokes equations something akin to an explosive instability could be observed. Before discussing the numerical work, however, let us first outline in slightly more detail the three articles just cited.

Goldstein & Lee (1992) considered the inviscid, long-wave limit of an adverse pressure gradient boundary layer taking the pressure gradient as a small parameter. Mallier & Maslowe (1994), on the other hand, treated resonant interactions in a hyperbolic tangent mixing layer and Wu (1992) analysed the Stokes layer. The scalings in all three of these studies were such that the form of the amplitude equation was dictated by the critical layer and that is why differences in the velocity profile outside the critical layer turn out to be only of secondary importance.

The basic disturbance in each of these three studies was composed of a plane wave plus a pair of oblique waves inclined at slightly less than $\pm 60^\circ$ to the mean flow direction. The frequency of the oblique modes was $1/2$ that of the plane wave and this configuration with the oblique modes inclined at exactly 60° would for a triad of *neutral* modes satisfy the resonance conditions exactly. (For boundary layers it is not generally possible to find such a triad of neutral modes, but the approximation is consistent with the long-wave limit considered in Goldstein & Lee.) This combination of modes was previously employed in the Blasius context and the reader is referred to § 17 of the monograph by Craik (1985) for an authoritative review of resonant interactions in shear flows. The wavenumbers were chosen to correspond with slightly amplified disturbances in order to yield a so-called non-equilibrium critical layer. Supposing that the initial amplitudes are infinitesimal, the plane wave on a linear

basis would have the largest amplification rate. However, this is true only initially because according to the amplitude equations derived in the forementioned papers a parametric resonance stage follows during which the amplification of the oblique waves is more rapid than exponential, whereas the plane wave continues to amplify at the rate predicted by linear theory until its amplitude is exceeded by that of the oblique waves. The rapid amplification of the oblique waves feeds back to the plane wave and the end result is a fully coupled system enhancing the growth rates of all the interacting modes. We have described this evolution in some detail because it will be seen that our numerical simulations follow quite closely this scenario. It should be noted that a similar analysis of the Blasius case by Mankbadi, Wu & Lee (1993) led to a different result, namely, that an oscillatory saturation stage followed the parametric resonance stage for the oblique waves.

Experiments on the transition of adverse pressure gradient boundary layers are few in number compared with the Blasius case. An extensive survey, primarily of research on flat-plate boundary layers, can be found in the review article by Kachanov (1994). A major contribution of the experimentalists was to underline the importance of three-dimensional effects once the initial stage of Tollmien–Schlichting instability is completed. The next stage includes spanwise-periodic longitudinal vortices and it was shown by Benney & Lin (1960) how these could be modelled by superimposing a pair of oblique waves on the primary plane wave disturbance. The details of exactly how this should be done was and still is a subject of some controversy.

In the Blasius boundary layer experiments, it was found that there are at least two distinct routes to turbulence. The so-called K-type of breakdown was investigated earlier than that characterized by subharmonic resonance. A significant difference between the two types of transition is that the oblique wave frequencies and wavenumber in the flow direction do not differ greatly from that of the plane wave in the K-type of interaction. Our simulations, however, concentrate on (but are not restricted to) the subharmonic instability mechanism because of its potential, as described above, for explosive instability. It was shown in the experiments of Saric & Thomas (1984) that for Blasius flow the forcing amplitude of the plane wave determined which scenario occurred. The initial amplitude of the plane wave leading to K-type breakdown was approximately double that in the subharmonic case, so it would seem that the latter is more characteristic of natural transition.

A first attempt to experimentally observe behaviour resembling the explosive instabilities predicted by the amplitude equations discussed above was reported recently by Corke & Gruber (1996). The velocity profiles in these experiments were well approximated by the Falkner–Skan similarity solutions of the boundary layer equations for flow over a wedge. The initial amplitudes, frequencies and obliqueness angles were all carefully controlled and the pressure gradients were relatively weak, corresponding to values of the Hartree parameter in the range $-0.06 \geqslant \beta_H \geqslant -0.09$ (the separation value is $\beta_H = -0.1988$). Although it could not be said that the instabilities were 'explosive', the transition process was none the less observed to differ from the Blasius case in some significant respects. For example, the region of nonlinear amplitude saturation immediately preceding transition was much shorter.

Our simulations will be seen in § 3 to agree well with the data reported by Corke & Gruber, the only noticeable difference being that we obtain slightly larger growth rates in the nonlinear régime. The primary motivation for our work, however, was to follow the evolution of resonantly interacting disturbances without being limited to small amplitudes and weak pressure gradients. That being the case the simulations at larger pressure gradients in § 3.2 should be of most interest. We find a substantial increase

in the amplification rates once the pressure gradient is stronger than $\beta_H = -0.10$. The paper concludes in §4 with a discussion of this and other results and suggests possible extensions of the research. First, however, we present the numerical methods employed in these computations and comparisons with linear theory that were used to validate the code.

2. Formulation and code validation

The Navier–Stokes equations are solved in this study using a vorticity–velocity formulation for the disturbance flow. The vorticity transport equations are coupled with an incompressibility constraint. The main appeal of the vorticity–velocity formulation is that the pressure variable is eliminated while the first-order continuity equation is replaced by additional second-order equations that are given below. The corresponding Stokes problem consists solely of seemingly independent, positive-definite equations for the vorticity and the velocity. However, this formulation requires that the boundary conditions for the vorticity equation be coupled with the solution for velocity. In numerical implementations based on this formulation, all boundary conditions are Dirichlet conditions so that the condition number for the system of equations is smaller than one with other types of boundary conditions. An accurate formulation of boundary conditions can then be achieved in a numerically compact way. Another attractive feature of the vorticity–velocity formulation is that the governing equations can be discretized on a non-staggered grid, thus allowing easy implementation. A more detailed discussion of the numerical scheme can be found in the thesis of the first author (Liu 1997).

Consider the flow past a semi-infinite flat surface which is inclined at an angle $\beta_H \pi/2$ to the incoming stream. Negative values of β_H correspond to positive angles of attack and, therefore, to a free-stream velocity

$$U_e^*(x^*) = U_o^* x^{\beta_H/(2-\beta_H)} \tag{2.1}$$

on the upper surface, where x is non-dimensional and x^* is dimensional; U_o^* is the free-stream velocity at the inflow boundary. The base flow, which develops under the adverse pressure gradient corresponding to equation (2.1), is represented by the velocity field $\boldsymbol{U} = (U, V, 0)$, where U and V are velocity components in the x- and y-direction, respectively, and the vorticity field $\boldsymbol{\Omega} = (0, 0, \Omega)$, where Ω is vorticity in the z-direction. For the disturbance flow, the velocity field is denoted by $\boldsymbol{u} = (u, v, w)$ and the vorticity field is $\boldsymbol{\omega} = (\omega_x, \omega_y, \omega_z)$. Then the vorticity–velocity equations for the disturbance flow are

$$\frac{\partial \boldsymbol{\omega}}{\partial t} = \nabla \times (\boldsymbol{u} \times \boldsymbol{\omega} + \boldsymbol{U} \times \boldsymbol{\omega} + \boldsymbol{u} \times \boldsymbol{\Omega}) + \frac{1}{R_o^*} \nabla^2 \boldsymbol{\omega}, \tag{2.2}$$

$$-\nabla^2 \boldsymbol{u} = \nabla \times \boldsymbol{\omega}. \tag{2.3}$$

The above equations are non-dimensionalized with respect to the free-stream velocity U_o^* and displacement thickness δ_o^* at the inflow station, and the kinematic viscosity v. The Reynolds number in (2.2) is then defined by $R_o^* = U_o^* \delta_o^* / v$.

At large Reynolds numbers, the base flow on a flat plate with pressure gradient can be accurately described by solutions of the boundary-layer equations. Although a marching algorithm may be used to solve the equations for the base flow, the widely used Falkner–Skan similarity profile is applicable when the free-stream velocity is of the form (2.1) and is employed for the present study. The profiles with different

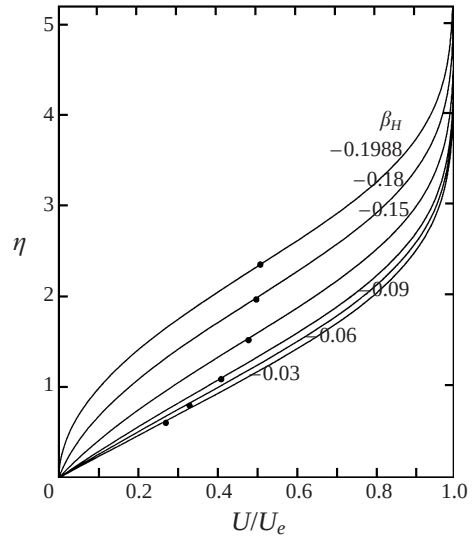

FIGURE 1. Mean velocity profiles; • indicates the point of inflection.

pressure gradients are shown in figure 1, where inflection points are indicated and η is a similarity variable defined as

$$\eta = y^* \left(\frac{U_e^*}{(2-\beta_H)\nu x^*} \right)^{1/2}.$$

The governing equations are solved in an integration domain extending in the x-direction from $x = x_0$ to $x = x_N$, where x_0 is the inflow boundary.

2.1. *Numerical scheme*

The integration domain in the y-direction extends from $y = 0$ to some large value of y, say $y = y_\infty$, and typically covers several boundary layer thicknesses. In the spanwise direction, the flow is assumed to be periodic with the domain extending from $z = 0$ to $z = \lambda_z$, because from boundary layer experiments it has been observed that a distinct periodic structure is evident in the spanwise direction. The buffer domain is appended to the end of the integration domain, thus providing a non-reflection outflow boundary treatment.

By exploiting the spanwise periodicity, a function can be written as a Fourier series expansion in the spanwise direction with wavenumber γ_z. (We will not study the final stage of breakdown into turbulence.) Furthermore, by selecting a set of $(\hat{\boldsymbol{u}}^o_{n,k}(y), \hat{\boldsymbol{\omega}}^o_{n,k}(y))$ properly, one can assume that u, v and ω_z are even functions expanded as cosine series, whereas w, ω_x and ω_y are odd functions expanded as sine series:

$$\{u, v, \omega_z\}(x, y, z, t) = \sum_{k=0}^{N_z} \{\hat{u}_k, \hat{v}_k, \hat{\omega}_{zk}\}(x, y, t) \cos(k\gamma_z z), \tag{2.4}$$

$$\{w, \omega_x, \omega_y\}(x, y, z, t) = \sum_{k=0}^{N_z} \{\hat{w}_k, \hat{\omega}_{xk}, \hat{\omega}_{yk}\}(x, y, t) \sin(k\gamma_z z). \tag{2.5}$$

Substituting (2.4) and (2.5) into (2.2) and (2.3) leads to a system of six equations for the kth harmonic in the (x, y) domain. The equations for the vorticity components

are

$$\frac{\partial \hat{\omega}_{xk}}{\partial t} = \frac{\partial \hat{P}_k}{\partial y} + \gamma_z k \hat{R}_k + \frac{1}{R_o^*}(\nabla_{xy}^2 - \gamma_z^2 k^2)\hat{\omega}_{xk}, \tag{2.6}$$

$$\frac{\partial \hat{\omega}_{yk}}{\partial t} = -\gamma_z k \hat{Q}_k - \frac{\partial \hat{P}_k}{\partial x} + \frac{1}{R_o^*}(\nabla_{xy}^2 - \gamma_z^2 k^2)\hat{\omega}_{yk}, \tag{2.7}$$

$$\frac{\partial \hat{\omega}_{zk}}{\partial t} = \frac{\partial \hat{R}_k}{\partial x} - \frac{\partial \hat{Q}_k}{\partial y} + \frac{1}{R_o^*}(\nabla_{xy}^2 - \gamma_z^2 k^2)\hat{\omega}_{zk}, \tag{2.8}$$

where $\hat{P}_k$, $\hat{Q}_k$ and $\hat{R}_k$ are the coefficients of the cosine series or sine series of the quantities P, Q and R, which have the definitions

$$P = u\omega_y - v\omega_x + U\omega_y - V\omega_x,$$
$$Q = v\omega_z - w\omega_y + V\omega_z + v\Omega,$$

and

$$R = w\omega_x - u\omega_z - U\omega_z - u\Omega.$$

The velocity components are related to the vorticity by

$$-\nabla_{xy}^2 \hat{u}_k + \gamma_z^2 k^2 \hat{u}_k = \frac{\partial \hat{\omega}_{zk}}{\partial y} - \gamma_z k \hat{\omega}_{yk}, \tag{2.9}$$

$$-\frac{\partial^2 \hat{v}_k}{\partial y^2} + \gamma_z^2 k^2 \hat{v}_k = \gamma_z k \hat{\omega}_{xk} + \frac{\partial^2 \hat{u}_k}{\partial x \partial y}, \tag{2.10}$$

$$-\frac{\partial^2 \hat{w}_k}{\partial y^2} + \gamma_z^2 k^2 \hat{w}_k = -\frac{\partial \hat{\omega}_{xk}}{\partial y} + \gamma_z k \frac{\partial \hat{u}_k}{\partial x}. \tag{2.11}$$

When starting the three-dimensional simulation, all disturbance variables $\hat{u}_k, \hat{v}_k, \hat{w}_k$, $\hat{\omega}_{xk}, \hat{\omega}_{yk}$, and $\hat{\omega}_{zk}$ are set to zero at $t = 0$. Then, for $t > 0$, the disturbances are introduced into the boundary layer at the inflow boundary. The disturbance forcing consists of a linear combination of eigenfunctions that are solutions of the Orr–Sommerfeld and Squire equations and it takes the form

$$(\boldsymbol{u}^o, \boldsymbol{\omega}^o) = \sum_n \sum_{k=-N_z}^{N_z} A_{n,k}^o \mathrm{Re}[(\hat{\boldsymbol{u}}_{n,k}^o(y), \hat{\boldsymbol{\omega}}_{n,k}^o(y)) \exp(\mathrm{i}(k\gamma_z z - nft))],$$

where $A_{n,k}^o$ are prescribed two- and three-dimensional disturbance amplitudes and f is a non-dimensional, real imposed disturbance frequency equal to $f^*\delta_o^*/U_e(x_o)$. The terms $\hat{\boldsymbol{u}}_{n,k}^o(y)$ are complex eigenfunctions normalized with respect to the maximum streamwise velocity component.

For the boundary condition at the wall, no-slip conditions are used for the velocity and the vorticity is computed from the most updated velocity. At the free-stream boundary, both the perturbation velocity and vorticity vanish exponentially, whereas the steady profile is that of a Falkner–Skan boundary layer. At the outflow boundary, the buffer domain technique (Joslin, Streett & Chang 1992) was used to prevent convective wave reflection or upstream propagation. Within this buffer domain, which has a length of approximately three wavelengths, the behaviour of the equations is parabolic rather than elliptic and it is added to the computational domain of interest. An attenuation function in this buffer region gradually reduces the streamwise viscous terms to zero and the boundary layer equations essentially apply at the outflow station.

A fractional step method is used in the time advancement. The nonlinear term and diffusion terms in the x- and y-directions are advanced by using a third-order

three-stage Runge–Kutta (RK) method (Williamson 1980). Implicit second-order Crank–Nicolson differencing is used for the normal diffusion term. This time-splitting procedure leads to the disturbance equations

$$\frac{\hat{\omega}^{\dagger}_{xk} - \hat{\omega}^{i-1}_{xk}}{h^i_t} = a^i H^i_{xk}(\hat{\boldsymbol{u}}, \hat{\boldsymbol{\omega}}), \tag{2.12}$$

$$\frac{\hat{\omega}^{\dagger}_{yk} - \hat{\omega}^{i-1}_{yk}}{h^i_t} = a^i H^i_{yk}(\hat{\boldsymbol{u}}, \hat{\boldsymbol{\omega}}), \tag{2.13}$$

$$\frac{\hat{\omega}^{\dagger}_{zk} - \hat{\omega}^{i-1}_{zk}}{h^i_t} = a^i H^i_{zk}(\hat{\boldsymbol{u}}, \hat{\boldsymbol{\omega}}), \tag{2.14}$$

and

$$\frac{\hat{\omega}^{i}_{xk} - \hat{\omega}^{\dagger}_{xk}}{h^i_t} = \frac{1}{2R^*_o}\frac{\partial^2}{\partial y^2}(\hat{\omega}^{\dagger}_{xk} + \hat{\omega}^{i}_{xk}), \tag{2.15}$$

$$\frac{\hat{\omega}^{i}_{yk} - \hat{\omega}^{\dagger}_{yk}}{h^i_t} = \frac{1}{2R^*_o}\frac{\partial^2}{\partial y^2}(\hat{\omega}^{\dagger}_{yk} + \hat{\omega}^{i}_{yk}), \tag{2.16}$$

$$\frac{\hat{\omega}^{i}_{zk} - \hat{\omega}^{\dagger}_{zk}}{h^i_t} = \frac{1}{2R^*_o}\frac{\partial^2}{\partial y^2}(\hat{\omega}^{\dagger}_{zk} + \hat{\omega}^{i}_{zk}), \tag{2.17}$$

where

$$\begin{pmatrix} H_{xk} \\ H_{yk} \\ H_{zk} \end{pmatrix}^i = \begin{pmatrix} L_{xk} \\ L_{yk} \\ L_{zk} \end{pmatrix}^{i-1} + b^i \begin{pmatrix} H_{xk} \\ H_{yk} \\ H_{zk} \end{pmatrix}^{i-1},$$

and

$$L_{xk} = \frac{\partial \hat{P}_k}{\partial y} + \gamma_z k \hat{R}_k + \left(\frac{\partial^2}{\partial x^2} - \gamma_z^2 k^2\right)\hat{\omega}_{xk},$$

$$L_{yk} = -\gamma_z k \hat{Q}_k - \frac{\partial \hat{P}_k}{\partial x} + \left(\frac{\partial^2}{\partial x^2} - \gamma_z^2 k^2\right)\hat{\omega}_{yk},$$

$$L_{zk} = \frac{\partial \hat{R}_k}{\partial x} - \frac{\partial \hat{Q}_k}{\partial y} + \left(\frac{\partial^2}{\partial x^2} - \gamma_z^2 k^2\right)\hat{\omega}_{zk}.$$

The quantity $\hat{\omega}^{\dagger}$ represents disturbance vorticities at the intermediate RK stages, $\hat{\omega}^{i-1}$ represents vorticities at previous RK stages ($i = 1, 2, 3$), $\hat{\omega}^0$ represents vorticities at the previous time step, and a^i,b^i and h^i_t are the RK coefficients and time steps, i.e.

$$\begin{pmatrix} a^1 & b^1 \\ a^2 & b^2 \\ a^3 & b^3 \end{pmatrix} = \begin{pmatrix} 1 & 0 \\ 9/4 & -5/9 \\ 32/15 & -153/128 \end{pmatrix} \quad \text{and} \quad \begin{pmatrix} h^1_t \\ h^2_t \\ h^3_t \end{pmatrix} = \begin{pmatrix} 1/3h_t \\ 5/12h_t \\ 1/4h_t \end{pmatrix},$$

where the sum of the three RK time stages equals the full time step h_t.

The solution procedure is as follows: the intermediate RK vorticities $\hat{\omega}^{\dagger}$ are determined by solving (2.12), (2.13) and (2.14) without imposing any boundary conditions for vorticities, whereas the boundary conditions at the wall and far field are needed for obtaining $\hat{\omega}^i$. Finally, velocities are obtained from (2.9), (2.10) and (2.11) with their boundary conditions. Upon solving the above system three consecutive times, full time step vorticities and velocities are determined. The main computer time consump-

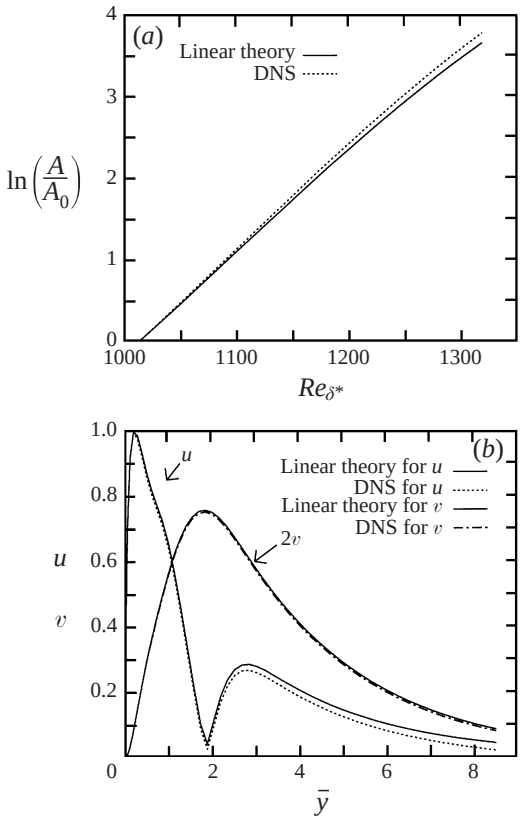

FIGURE 2. Comparison of the numerical results with linear theory for $\beta_H = -0.09$, $F = 96$ and $\alpha = 0.2757 - \mathrm{i}\,0.0244$: (*a*) amplification curves; (*b*) amplitude distribution (normalized by u_{max}) u, and v.

tion is in solving the Helmholtz equations for the velocity components and vorticity components.

Spectral element methods are high-order weighted-residual techniques for partial differential equations that combine the geometric flexibility of finite element techniques with the rapid convergence rate of spectral schemes (Korczak & Patera 1986; Mavriplis 1989). In the spectral element discretization, the computational domain is broken up into elements, and the dependent and independent variables are approximated by Nth-order tensor-product element-based polynomial expansions. Both the variational principle and Gaussian numerical quadrature are used to form the discrete equations of the velocity components and vorticity components. The preconditioned conjugate gradient method was used to avoid forming matrices of the discrete equations and improve the convergence rate. This leads to a significant reduction in the computational demands.

2.2. *Code validation*

The code validation was done by comparing the numerical results with results from linear stability theory and many examples can be found in Liu (1997). We show here only one such comparison, a calculation performed for a Falkner–Skan boundary layer with $\beta_H = -0.09$. In the streamwise direction, the computational domain, which consists of three to four wavelengths, extends from x_0, where the Reynolds number is

$Re_{\delta^*}(x_0) = 1012$, to x_N, where the Reynolds number is $Re_{\delta^*}(x_N) = 1329$. In the (x, y)-plane, the computational domain with the buffer domain is subdivided into $8 \times 5 \times 5$ elements. In each element $(N_x + 1) \times (N_y + 1) = 9 \times 9$ of Legendre–Gauss–Lobatto points are used. As a result, the total number of points is 13161. The base flow was disturbed by a two-dimensional wave with frequency parameter $F = 96$, where $F = (f/R_o^*) \times 10^6$ and R_o^* is the inflow Reynolds number defined earlier. Figure 2 shows the comparison of amplification curves and the amplification distribution for u and v. The independent variable is $\bar{y} = y\delta^*(x_0)/\delta^*(x)$. For the sake of clarity the distributions of $2v$ instead of v were plotted. The agreement with linear theory is seen to be very good. In figure 2(*a*), the amplification rate is slightly higher than that of linear theory, but that is expected owing to non-parallel effects. The Reynolds number is increasing in the downstream direction and the perturbation is consequently moving into a region of larger amplification rate. These effects are, of course, included in the DNS, but not in the linear Orr–Sommerfeld stability theory. What is essential is that the initial slopes of the two curves in figure 2(*a*) agree.

3. Numerical results

Detailed measurements in adverse pressure gradient boundary layers are available only for small pressure gradients and this section begins by comparing some of these data with our numerical simulations. In the experiments of Corke & Gruber, the oblique waves were always forced at an inclination of $\pm 60^\circ$ to the mean flow. We consider in § 3.1 the slightly smaller angles for which the subharmonic resonance conditions are satisfied, but we also investigate the effect of varying this angle. Then, in § 3.2 larger pressure gradient cases are examined in some detail; for $\beta_H = -0.18$ results are compared for triads satisfying the subharmonic resonance condition with those corresponding to a Benney–Lin triad. Intermediate values of β_H are also considered and the maximum disturbance amplitudes are determined as a function of pressure gradient. Finally, in § 3.3, perturbations consisting of an oblique wave pair with no plane wave present initially are considered.

3.1. *Comparison with experiment*

The data presented in Corke & Gruber (1996) were for two values of the Hartree parameter, namely, $\beta_H = -0.06$ and $\beta_H = -0.09$. In our simulations, the choice of dimensionless frequency $F = 96$ for the basic plane wave disturbance was made to coincide with the experimental value. The oblique subharmonics and plane wave were all introduced at the inflow station; the oblique waves have a frequency $F = 48$ and are periodic in the spanwise direction. The initial Reynolds numbers based on displacement thickness were 987 and 1012, respectively, large enough to be in the linearly unstable range and the wavenumber in the flow direction was chosen to be the most amplified according to linear theory. The wavenumber in the spanwise direction was obtained by finding solutions of the Orr–Sommerfeld equation such that the resonance conditions were satisfied. In the present context, this means that the phase speeds of the plane and oblique waves are identical. The spanwise wavenumbers satisfying the latter condition turn out to be 0.1665 and 0.1758 in the cases of $\beta_H = -0.06$ and $\beta_H = -0.09$, respectively. As the disturbances propagate downstream, there will be some detuning owing to boundary layer growth and finite-amplitude effects, but this detuning seems to be small within the domain studied.

The resulting angle of inclination to the basic flow direction for subharmonic resonance is between 51° and 52°. This is somewhat less than the asymptotic value of

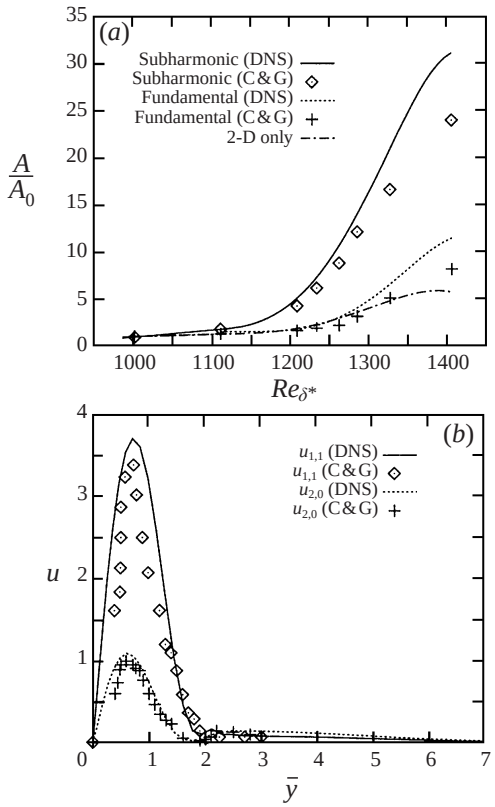

FIGURE 3. Comparison of the numerical results with measurements by Corke & Gruber (C & G) for $\beta_H = -0.06$ and $\alpha = 0.2684 - \mathrm{i}\,0.0173$: (*a*) streamwise growth of maximum *u*-fluctuations; (*b*) *u*-amplitude distribution at $Re_{\delta^*} = 1233$.

60° used in the analysis of Goldstein & Lee (1992) and in the experiment by Corke & Gruber. It will be seen below that this small difference noticeably affects the results. The inflow amplitudes of the fundamental and subharmonic wave are 0.41% and 0.36% for the case $\beta_H = -0.06$ and 0.27% and 0.12% for the case $\beta_H = -0.09$. To be consistent with ideas related to Squire's theorem, we have set the initial amplitude of the subharmonic wave to be slightly smaller than that of the fundamental wave.

The fundamental (two-dimensional) and subharmonic (three-dimensional) disturbance components are denoted as modes (n_t, n_z) and the corresponding amplitudes are A_{n_z,n_t}, where n_t stands for the frequency as a multiple of the subharmonic frequency and n_z denotes a multiple of the spanwise wavenumber. For example, the two-dimensional fundamental wave is denoted as mode (2,0) and the three-dimensional subharmonic wave is denoted as mode (1,1). For comparison with each mode of the experiments, the numerical results are Fourier analysed in time for every x, y and z location.

Results of the calculations for the case $\beta_H = -0.06$ are shown in figure 3. The value of α given in the figure caption is that of the plane wave; the corresponding value of α_r for the oblique waves in all subharmonic interaction cases was 1/2 that of the plane wave. The results presented here are from a Fourier analysis of the eighth time period after the disturbance was initiated at the inflow boundary. Figure 3(*a*) shows the streamwise growth of maximum *u*-fluctuations. Amplitudes of both the

fundamental and subharmonic modes in the computations have been normalized by $A_{2,0}(x_0)$. Generally, agreement with the experiments is quite good. Before discussing these comparisons, however, it is interesting to note the behaviour of the plane wave in the simulations when the oblique waves are absent. This is shown in the lowest curve of figure 3(*a*) where it can be seen that nonlinear saturation occurs before there is very much amplification. Itoh (1974) has carried out a Stuart–Landau analysis for the Blasius boundary layer that predicts finite-amplitude equilibration in accordance with our computations suggesting that his conclusions are qualitatively valid even for small pressure gradients.

The other curves describe the resonantly interacting modes and are the ones of primary interest. It is particularly noteworthy that the oblique subharmonics, contrary to Squire's theorem, are the most amplified almost from the beginning. For Reynolds numbers less than 1250, a sort of parametric resonance occurs in which the plane wave's evolution is hardly affected by the presence of the oblique modes; this is true even when the amplitude of the oblique waves is double that of the plane wave, as predicted by the amplitude equations discussed in § 1. The oblique waves, on the other hand, amplify at a much greater rate than would be the case if the plane wave were absent. At higher Reynolds numbers, the modes interact strongly and the rapid amplification of the oblique waves feeds back to the plane wave and enhances its growth rate. The amplitude ratio of the subharmonic mode to the fundamental mode at the most downstream position in the computation is 2.72 compared with a ratio of 2.9 in the experiment.

The mean flow generated by the interaction of the oblique waves, i.e. the (0,2) mode, turns out to be less significant in the triad interaction than when the plane wave is absent. It has been omitted from figure 3(*b*) for reasons of clarity, but it would be nearly coincident with the curve labelled two-dimensional only and slightly below it.

Amplitude distributions with respect to $\bar{y}$ of the numerical results and experiments are compared in figure 3(*b*) for $Re_{\delta^*} = 1233$. To demonstrate the quantitative difference between the subharmonic and fundamental mode, the curves were normalized by the $u_{2,0}$ maximum of experimental measurements. Except for some deviation close to the maxima, the agreement between simulation and experiment for both modes is very good.

Similar comparisons for $\beta_H = -0.09$ have also been made. Figure 4(*a*) compares the maximum u-fluctuations predicted by computation with the experimental measurements of Corke & Gruber. For this case, the quantitative agreement is again quite good between the experimental data and numerical results for the growth rates of the fundamental and subharmonic modes. The amplitude ratio at the most downstream position is 1.46 by computation and 1.3 in the measurements. Note that in the Blasius flow experiments of Corke & Mangano (1989) the amplitude ratio was found to be about 5, so this quantity decreases rapidly with increasing pressure gradient and it will be seen below that the trend continues as β_H becomes more negative.

Figure 4(*b*) compares the u-component amplitude variation as a function of height. It has been observed experimentally that for moderate adverse pressure gradients a double peak in this quantity occurs. The double peak is evident in figure 12(*b*) of Corke & Gruber with $\beta_H = -0.09$ and in figure 1 with $\beta_H = -0.18$ in Hest, Passchier & Henkes (1996). The same feature appears in our computations as can be seen in figure 4(*b*). Although the computed amplitude evolution, as illustrated in both figures 3(*a*) and 4(*a*), follows quite closely the measurements of Corke & Gruber, it can be seen that at the more downstream stations the computed growth rates are noticeably

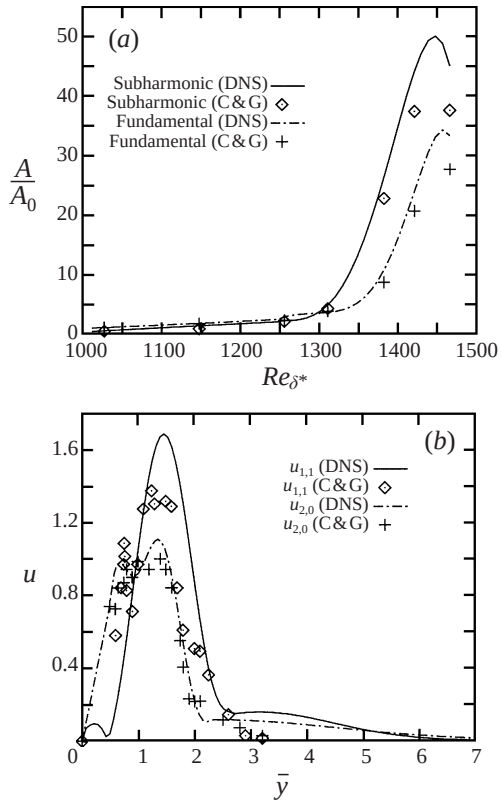

FIGURE 4. Comparison of the numerical results with measurements by C & G for $\beta_H = -0.09$: (*a*) streamwise growth of maximum *u*-fluctuations; (*b*) *u*-amplitude distribution at $Re_{\delta^*} = 1466$.

greater. This is true for both the plane wave and the subharmonics. It turns out that the discrepancy can be explained by taking into account the angle of inclination of the oblique subharmonics. In the case of Blasius flow, Zelman & Maslennikova (1993) using weakly nonlinear methods were able to predict with some degree of success the obliqueness angle that would give rise to the largest growth rate.

We have carried out a similar investigation, but based on the full equations, for the mean flow with $\beta_H = -0.09$. In these simulations, the oblique waves no longer satisfy the resonance conditions so we do not use Orr–Sommerfeld modes for them at the inflow boundary. Instead, we employ the procedure of Fasel, Rist & Konzelmann (1990) to simulate disturbances introduced by localized blowing and suction within a narrow strip $x_1 \leqslant x \leqslant x_2$. For this, the normal velocity component is chosen as

$$\hat{v}_k(x,0,t) = A^o_{n,k}\sin(\alpha_{rk}(x-x_1))\sin(f_n t), \qquad x_1 \leqslant x \leqslant x_2,$$
$$\hat{v}_k(x,0,t) = 0, \qquad x_0 \leqslant x < x_1 \text{ and } x_2 < x \leqslant x_N,$$

where $A^o_{n,k}$, f_n and α_{rk} are real constants that can be chosen to adjust the initial amplitude, the frequency and wavenumber of disturbances. The width of the suction strip, $x_2 - x_1$, for these calculations is two wavelengths of the fundamental mode or one wavelength of the subharmonic mode. The location of x_1 is approximately one fundamental wavelength downstream of the inflow boundary.

In figure 5, we show the dependence of subharmonic growth rate on obliqueness an-

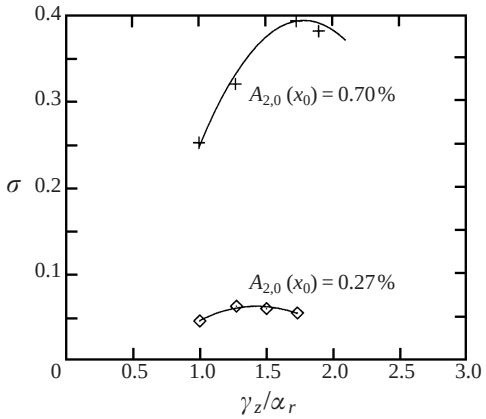

FIGURE 5. Effect of wavenumber ratio on the subharmonic mode amplification rate with $\beta_H = -0.09$ and $Re_{\delta^*} = 1300$.

gle. The two curves demonstrate that the outcome depends on the initial amplitude of the plane wave. For the lower curve, the initial amplitude of the plane wave was set to be $A_{2,0} = 0.27\%$ and four cases were run; the lowest ratio of the spanwise wavenumber to streamwise wavenumber was 1 and the largest was 1.732. The subharmonic growth rate, denoted σ in figure 5, is analogous to the quantity $A^{-1}\mathrm{d}A/\mathrm{d}x$ defined in (3.5) of Zelman & Maslennikova. The use of a locally linearized quantity is less appropriate in the more nonlinear computations depicted here, but it is convenient for presentation as it facilitates comparison with figure 6(*b*) of Zelman & Maslennikova dealing with the Blasius boundary layer. However, the true amplification rate is faster than exponential, so σ increases with x.

For the smaller amplitude case, it can be seen that the largest amplification rate occurs when the input obliqueness angle is close to the 51° value predicted by resonant interaction theory. However, when the initial amplitude of $A_{2,0}$ is increased to 0.7%, then the largest growth rate is obtained when the oblique modes are inclined at approximately 60°. This result is not necessarily inconsistent with resonant interaction theory; rather, it indicates that higher-order terms need to be taken into account when the initial amplitude of the plane wave is larger. The latter situation is a favourable one for secondary instability approaches, such as those reviewed by Herbert (1988) and, possibly, they offer an easier alternative to predicting the obliqueness angle giving the largest initial growth rate. The controversial Squire modes (see discussion in § 26.1 of Craik 1985 and § 3.4 of Zelman & Maslennikova) might also play a role, but it seemed unlikely to us that these linearly damped modes would be of primary importance, so we have done no calculations in which they were included.

The trends illustrated in figure 5 are similar to those for the Blasius boundary layer treated in Zelman & Maslennikova, as indicated above. These authors have also obtained some results for the case $\beta_H = -0.10$ and they found, in contrast with the flat-plate and favourable pressure gradient cases, that the dependence of growth rate on obliqueness angle varies with Reynolds number. This suggests that the optimal obliqueness angle may vary with a number of parameters and the question deserves a more detailed investigation.

In the experimental data in figures 3(*a*) and 4(*a*), the oblique waves were forced at 60° in order to coincide with the long-wave limit treated by Goldstein & Lee (1992). Initially, we just assumed that this accounts for the difference in growth rates when

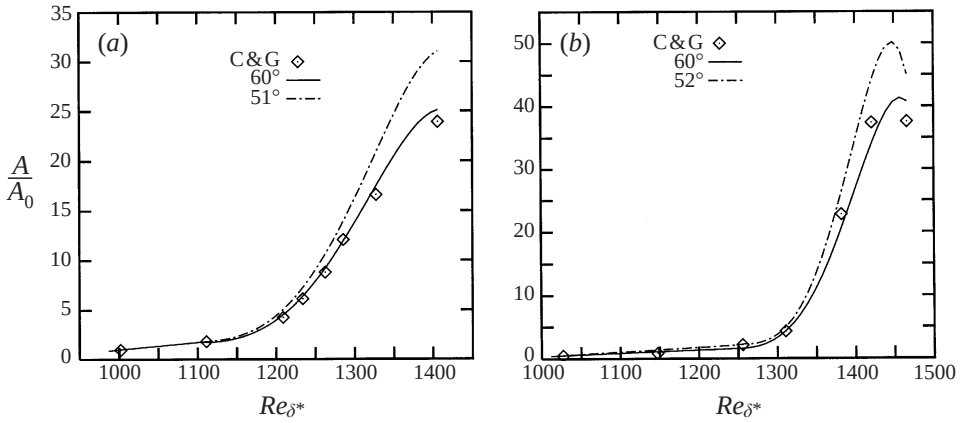

FIGURE 6. Comparison of the numerical results with measurements by C & G with the different oblique angles (*a*) $\beta_H = -0.06$, (*b*) $\beta_H = -0.09$.

compared with the simulations done at 51°. However, at the suggestion of a referee, we repeated these computations employing oblique waves inclined at 60° and the new results are shown in figure 6. The agreement with the experiments is remarkable, especially when taking into account that it is not possible to simulate exactly a Falkner–Skan flow experimentally. A 'virtual leading edge' must be employed so there is some uncertainty as to the equivalent Reynolds number. Perhaps the excellent agreement means that the stability properties are not particularly sensitive to the Reynolds number. In any case, these results suggest that forcing the oblique waves at 51° in the experiments would have produced even larger amplification rates than those observed.

When the initial amplitudes are small, figure 5 shows that the largest growth rates occur when the resonance conditions are satisfied exactly. We have computed the spatial growth for the 45° case, i.e. the first point on the lower curve in figure 5. For reasons of clarity, we did not show this curve in figure 6; however, for $Re_{\delta^*} > 1300$ it lies below that for the 60° case.

3.2. *Stronger pressure gradients*

Figure 7 illustrates the evolution of the disturbance amplitudes in a case with a stronger pressure gradient, namely, $\beta_H = -0.12$. A significant increase in the amplification rate was observed at this value of β_H. Owing to the rapid amplification of both primary and subharmonic disturbances, the logarithm of the amplitudes is plotted rather than the amplitudes themselves. This is the first case where the amplification is great enough to warrant a comparison with the predictions of the evolution equations discussed in § 1. However, it is clear that the singular behaviour exhibited in figure 2, for example, of Goldstein & Lee (1992) does not occur in the numerical simulation. We must conclude, therefore, that the theory breaks down shortly after the fully coupled stage is reached.

We do not know of any experiments that would be able to confirm or contradict the relatively sudden increase in amplification rate observed in our simulations when the pressure gradient becomes stronger than $\beta_H \approx -0.10$. It is likely that experiments have been done at the pressure gradients of interest here, but such results do not seem to have been published in sources accessible to us and so we are unable to make comparisons. Linear theory, incidentally, cannot account for the above mentioned

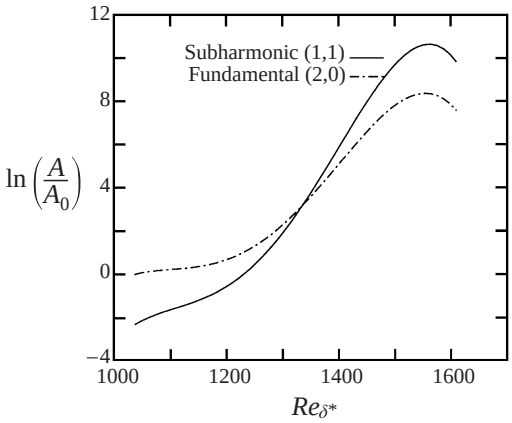

FIGURE 7. Streamwise growth of maximum u-fluctuations for $\beta_H = -0.12$ and $\alpha = 0.2834 - \mathrm{i}\,0.0337$.

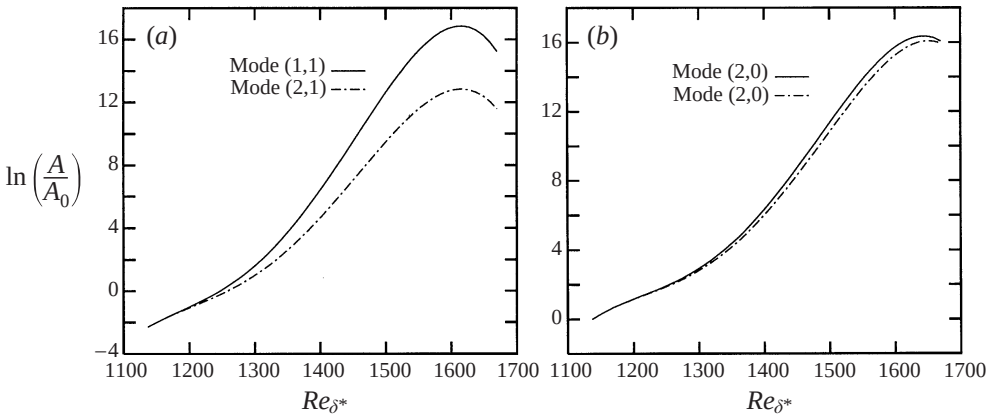

FIGURE 8. Streamwise growth of maximum u-fluctuations for $\beta_H = -0.15$ and $\alpha = 0.3093 - \mathrm{i}\,0.0483$: (*a*) three-dimensional modes; (*b*) two-dimensional modes. Solid line for subharmonic breakdown; dashed line for fundamental breakdown.

rapid variation with pressure gradient. Figure 12 of Obremski, Morkovin & Landahl (1969) shows the increase of the maximum value of $-\alpha_i$ as $-\beta_H$ increases and the variation is gradual, so nonlinear effects must be responsible for our results.

Some numerical simulations, however, were reported for the case $\beta_H = -0.18$ by Kloker & Fasel (1990). These authors found that a larger growth rate was obtained for the oblique waves than in the subharmonic case when the oblique waves had the same frequency as the plane wave (this is termed 'fundamental breakdown' in their report). We were rather skeptical about this conclusion because the triad resonance conditions are not satisfied in the fundamental configuration. Our own simulations did in fact support the results of Kloker & Fasel to the extent that larger growth rates were obtained than anticipated. However, as shown in figure 8 for $\beta_H = -0.15$ and in figure 9 for $\beta_H = -0.18$, although the plane wave saturation amplitudes are comparable, the oblique waves attain significantly larger amplitudes when the subharmonic resonance conditions are satisfied.

Two possible explanations for the discrepancy come to mind. The first is computatational: the outflow boundary conditions employed in Kloker & Fasel appear to

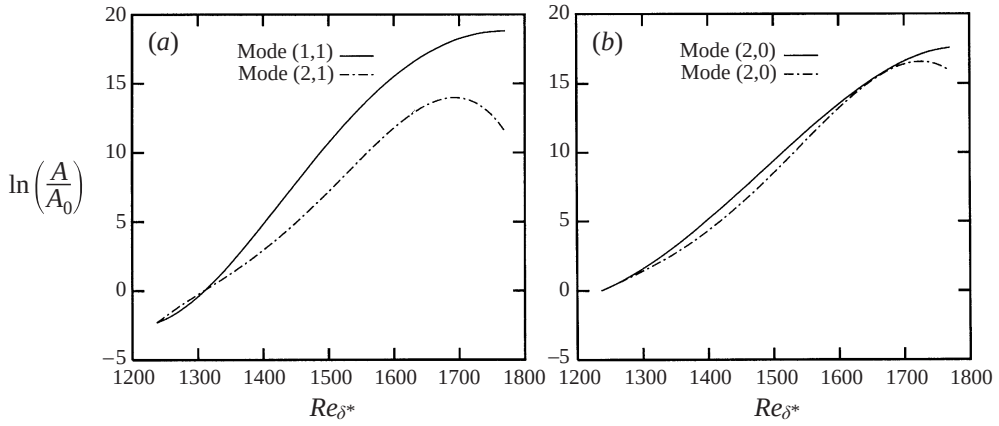

FIGURE 9. Streamwise growth of maximum u-fluctuations for $\beta_H = -0.18$ and $\alpha = 0.3377 - \mathrm{i}\,0.0861$: ($a$) three-dimensional modes; (b) two-dimensional modes. Solid line for subharmonic breakdown; dashed line for fundamental breakdown with oblique wavenumber $\alpha = 0.3171 - \mathrm{i}\,0.0812$ and $\gamma_z = 0.2354$.

be quasilinear and assume spatial periodicity which would be less accurate than the use of a buffer domain. It was, in fact, reported by Fasel *et al.* (1990, p. 34) that these conditions led to numerical difficulties in cases with large amplification. Also, they used only two modes in the spanwise coordinate, whereas we used five. A second possibility is differences in initial conditions because Kloker & Fasel chose the initial amplitude of the oblique waves to be double that of the fundamental. (We have since discussed this with Professor Fasel and the input conditions actually used were the reverse of what is stated in the paper.) Irrespective of these differences, it is interesting that the fundamental disturbance configuration does lead to sizeable amplification in the case $\beta_H = -0.18$ and there is a tentative suggestion that both types of resonance were present in experiments reported by Hest *et al.* at the same value of β_H.

Some theoretical support and a possible explanation can be found in a recent article by Mallier (1995) on Benney–Lin triads in mixing layers. Mallier has derived amplitude equations with finite-time singularities governing interactions where the plane wave is larger in order of magnitude than the oblique waves. Even though his calculations are for a $\tanh y$ mixing layer, the conclusions may be applicable to the near-separation boundary layer because of the inflectional velocity profile present in both cases.

In figure 10, the maximum amplitudes are shown as a function of the Falkner–Skan parameter β_H. The frequency parameters for the plane and oblique modes were $F = 96$ and $F = 48$ in all cases. As noted above, a dramatic increase in amplification rate occurs at $\beta_H = -0.12$ and this translates into a correspondingly large maximum amplitude. This trend continues with increasing pressure gradient; in fact, the disturbances were still growing when the computation was terminated in the case $\beta_H = -0.18$ illustrated in figure 9. No doubt, the flow would break down into turbulence at this point. Unfortunately, the resolution in our numerical scheme is not adequate to resolve the small scales that arise in the final stage of breakdown.

3.3. *Oblique wave disturbance pairs*

A perturbation composed of a pair of oblique waves can amplify significantly even in the absence of a plane wave. The instability mechanism involves a resonance with

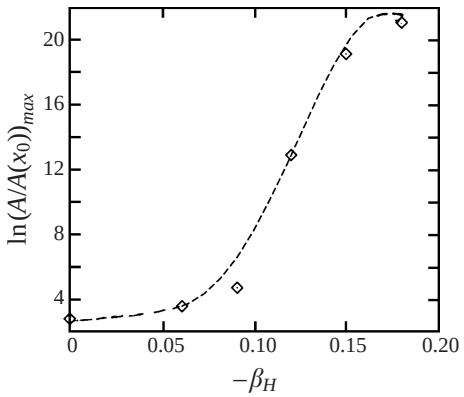

FIGURE 10. Variation of the maximum subharmonic amplitude with β_H.

the mean flow and its strength is enhanced by the stronger critical point singularity that occurs in the inviscid limit compared with a single plane wave mode. Benney (1961) showed that in the nearly-neutral case this resonance can produce a secondary flow whose u-component velocity grows like t^2, while the mean longitudinal vorticity component grows linearly in t. Some spatial simulations for the Blasius boundary layer were reported by Joslin, Streett & Chang (1993) who found that the outcome depended on the initial amplitudes. Only for relatively large initial amplitudes did the disturbance amplify sufficiently for the authors to state that breakdown was indicated. Similar computations by Berlin, Lundbladh & Henningson (1994) led to different conclusions. These authors have simulated bypass transition with initial oblique wave perturbations of comparable amplitude to those employed by Joslin *et al.* and attribute the different outcome to a variation in the initial input concerning the normal vorticity. However, our communications with these authors indicate that the discrepancy is due in part to different criteria being employed to define 'transition'.

Although the differing conclusions in these articles seem deserving of further investigation in the Blasius case, our own results suggest that the oblique wave pair instability is not competitive with the subharmonic triad when there is a pressure gradient. We have made several runs at the two values of the Falkner–Skan parameter $\beta_H = -0.06$ and -0.15. Our results are similar to those of Joslin *et al.* in that there is a strong dependence on initial amplitude. Figure 11(a) illustrates the oblique wave amplification in the case $\beta_H = -0.06$ which is seen to be unimpressive. It is more interesting to observe that the streamwise vortex component, which is absent initially, grows in accordance with the predictions of Benney (1961) and soon becomes larger than the oblique waves. A plane wave is also generated immediately by weak nonlinear interaction of the oblique waves, but its amplitude remains smaller.

Figures corresponding to other cases involving oblique wave pairs can be found in the thesis of the first author (Liu 1997), but here we provide only a brief description. For initial amplitudes smaller than the simulation in figure 11 there is virtually no amplification of the oblique waves, but the (0,2) vortex component still shows some growth. At the stronger pressure gradient $\beta_H = -0.15$, all modes grow to an amplitude that is substantial, but none the less is only about 20% of the maximum amplitudes reached in the subharmonic triad interaction. Moreover, the subharmonic triad does not require special initial amplitudes to yield rapid disturbance growth, so we believe that it is more pertinent to natural transition.

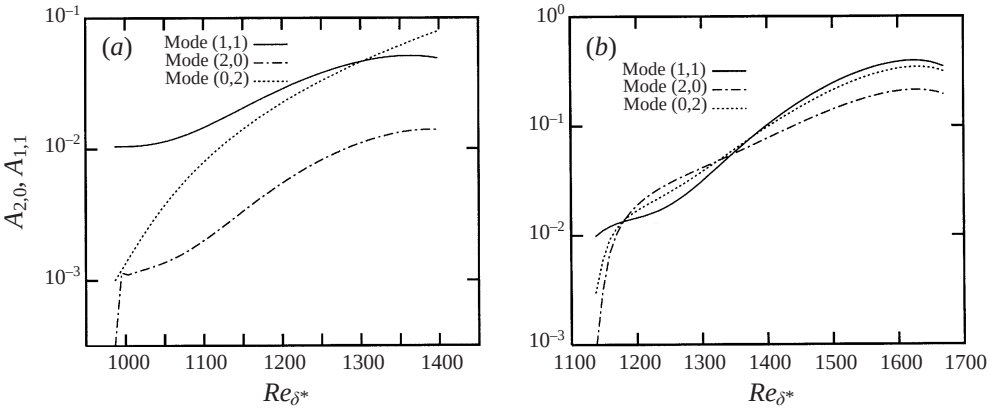

FIGURE 11. Streamwise growth of maximum u-fluctuations from an oblique wave pair: (*a*) $\beta_H = -0.06, A_{1,1}(x_0) = 1.0\%$; (*b*) $\beta_H = -0.15, A_{1,1}(x_0) = 0.10\%$.

4. Concluding remarks

In the preceding section, DNS simulations were presented for several interacting wave configurations and we considered values of the pressure gradient parameter ranging from almost flat-plate conditions to near separation. Although our investigation is the most comprehensive to date in this respect, it is clear that much remains to be done owing to the large number of parameters that can be varied in the problem. For the most part, we concentrated on initially small disturbances because we were interested in natural transition and we employed subharmonic resonant triad perturbations because these led to the largest growth rates.

Possibly our most surprising finding was that there is a substantial increase in nonlinear amplification rate occurring somewhere in the range $-0.12 \leqslant \beta_H \leqslant -0.09$. The character of transition seems to change abruptly as the pressure gradient increases near those values of the Hartree parameter. The experiments of Corke & Gruber (1996) failed to exhibit the explosive instability predicted in the theoretical work discussed in § 1, but the results presented herein suggest that an extension of those experiments to slightly larger pressure gradients might lead to instabilities that could be so-characterized in that very large growth rates occur.

One question that is raised by our computations is why the amplification rates increase so dramatically with pressure gradient? Although none of the theoretical work discussed in § 1 is directly applicable in the parameter range of most interest here, there are indications that critical layer dynamics dominate much of the transition process. On p. 168 of the monograph by Craik (1985), the factors contributing to large coefficients of the nonlinear terms in the amplitude equations governing weakly nonlinear resonant interactions are discussed. Distance of the critical layer from the wall is one of those factors and, as is clear from figure 1 of this paper, the critical layer (which is not far from the inflection point in the velocity profile) moves away from the wall rapidly with increasing pressure gradient. Even though Craik's asymptotic analysis is not valid in the parameter régime where most of our computations were performed, it is still to be expected that the wall has a damping influence on instabilities originating in the critical layer. If that is the case, then an increased distance of the critical layer from the wall and shorter-wavelength disturbances will be associated with larger growth rates. The importance of the wavelength is clear from the Blasius flow interaction coefficients computed by Hendricks, the results of

which are given in the appendix to Usher & Craik (1975). Increasing α from 0.1 to 0.5 radically changed the relative values of the coefficients of the nonlinear terms in the amplitude equations, with the larger wavenumber indicating rapid amplification of the oblique subharmonics.

A number of viewpoints besides that of resonant triads have been proposed as candidates for assessing transition in Blasius boundary layers and other shear flows. We have said little about these, but a few words about the closely related topic of secondary instability are appropriate in the light of our results. A review of different formulations of resonant interaction theory, as well as the parametric approach to secondary instability theory, can be found in a paper by Nayfeh (1987), whereas the survey article by Herbert (1988) deals primarily with secondary instability. Although secondary instability theories are subject to the limitations of any linear theory, they are believed capable of predicting quantities such as observed wavenumbers of secondary bifurcations. In order to do this, it is necessary that the primary instability first attain a quasi-equilibrium state; experiments on Blasius boundary layers, as well as mixing layers, indicate that assumption to be a reasonable one. Our simulations presented in this article, however, demonstrate that such behaviour is not to be expected for moderate presure gradients. In the case of a small adverse pressure gradient, a Floquet-type of analysis should provide reliable results for a certain distance. But even for $\beta_H = -0.06$, figure 3(a) indicates that the evolution of the plane and oblique modes becomes coupled and once there is feedback from the subharmonic to the primary disturbance, the latter resumes its amplification. The non-equilibrium critical layer formulation of Goldstein & Lee (1992) does incorporate the effects of coupling and at least for small pressure gradients provides a picture consistent with our results for some distance beyond the parametric stage and extending into the nonlinear régime. However, the behaviour near the singularity of the nonlinear amplitude equations suggests that the plane wave blows up more rapidly than the oblique waves and that is not consistent with our results.

Some comments on the computational aspects of this investigation should also be added. The simulations presented here were done on a workstation and represented the maximum load that could be handled on such a machine. Spatial simulations are much more demanding than those utilizing a temporal approach. However, we believe that for the present problem a spatial formulation is necessary for a number of reasons. One is that the dispersive properties of spatial and temporal modes are not the same. Because we are concerned with resonant interactions, it is important to maintain the same relationship between propagation speeds and wavelengths as in the real world. A consequence, however, of doing spatial simulations is the need for a reliable outflow boundary condition. The use of a buffer domain greatly increases the computing requirements, but was found necessary to obtain satisfactory results. The formulation of more efficient outflow conditions is a subject of ongoing research and progress anticipated in this area will greatly facilitate computational stability investigations extending the present effort.

To summarize our conclusions, of the numerous factors influencing the evolution of resonantly interacting waves in a boundary layer, the results presented in § 3 show that the outcome is particularly sensitive to the streamwise pressure gradient. This is not surprising if we recall that even on a linear basis two different instability mechanisms can be involved and which one is dominant depends primarily on the pressure gradient. In the Blasius limit of zero pressure gradient, the viscous Tollmien–Schlichting mechanism is responsible for instability. However, at moderate values of the (adverse) pressure gradient a quite different, essentially inviscid, mechanism is

responsible for the instability and viscosity can be stabilizing; the latter mechanism is a consequence of a vorticity maximum in the velocity profile and is discussed in § 4.4 of Lin (1955). The initial amplitudes of plane and oblique modes, as well as their ratio, no doubt are also important, and other types of disturbances may be present in experiments with forcing. Clearly, transition in shear flows involves a number of possible scenarios and we do not put the emphasis on any 'universal' feature; rather, it is the differences between each case that makes the subject so fascinating.

We are greatly indebted to Professor Thomas Corke for discussions of his experimental work, his encouragement and even for helpful suggestions about numerical aspects. We have also benefited from stimulating discussions with Dr Marvin Goldstein and we thank him for his continued interest. This research was supported by the Natural Sciences and Engineering Research Council of Canada.

REFERENCES

Benney, D. J. 1961 A nonlinear theory for oscillations in a parallel flow. *J. Fluid Mech.* **10**, 209–236.

Benney, D. J. & Lin, C. C. 1960 On the secondary motion induced by oscillations in a shear flow. *Phys. Fluids* **3**, 656–657.

Berlin, S., Lundbladh, A. & Henningson, D. 1994 Spatial simulations of oblique transition in a boundary layer. *Phys. Fluids* A **6**, 1949–1950.

Corke, T. C. & Gruber, S. 1996 Resonant growth of three-dimensional modes in Falkner–Skan boundary layers with adverse pressure gradients. *J. Fluid Mech.* **320**, 211–233.

Corke, T. C. & Mangano, R. A. 1989 Resonant growth of three-dimensional modes in transitioning Blasius layers. *J. Fluid Mech.* **209**, 93–150.

Craik, A. D. D. 1985 *Wave Interactions and Fluid Flows.* Cambridge University Press.

Fasel, H. F., Rist, U. & Konzelmann, U. 1990 Numerical investigation of the three-dimensional development in boundary-layer transition. *AIAA J.* **28**, 29–37.

Goldstein, M. E. & Lee, S. S. 1992 Fully coupled resonant-triad interaction in an adverse-pressure-gradient boundary layer. *J. Fluid Mech.* **245**, 523–551.

Herbert, Th. 1988 Secondary instability of boundary layers. *Ann. Rev. Fluid Mech.* **20**, 487–526.

Hest, B. F. A. van, Passchier, D. M. & Henkes, R. A. 1996 Natural transition in an adverse pressure gradient boundary layer. *Advances in Turbulence VI* (ed. S. Gavrilakis *et al.*), pp. 395–398. Kluwer.

Itoh, N. 1974 Spatial growth of finite wave disturbances in parallel and nearly parallel flows. Part 2. The numerical results for the flat plate boundary layer. *Trans. Japan Soc. Aero Space Sci.* **17**, 175–186.

Joslin, R. D., Streett, C. L. & Chang, C.-L. 1992 Validation of three-dimensional incompressible spatial direct numerical simulation code: a comparison with linear stability and parabolic stability equation theories for boundary-layer transition on a flat plate. *NASA TP* 3205.

Joslin, R. D., Streett, C. L. & Chang, C.-L. 1993 Spatial direct numerical simulation of boundary-layer transition mechanisms: validation of PSE theory. *Theor. Comput. Fluid Dyn.* **4**, 271–288.

Kachanov, Y. S. 1994 Physical mechanisms of laminar-boundary-layer transition. *Ann. Rev. Fluid Mech.* **26**, 411–482.

Kloker, M. & Fasel, H. 1990 Numerical simulation of two- and three-dimensional instability waves in two-dimensional boundary layers with streamwise pressure gradient. *Laminar-Turbulent Transition* (ed. D. Arnal & R. Michel), pp. 681–686. Springer.

Korczak, K. Z. & Patera, A. T. 1986 An isoparametric spectral element method and its application to incompressible two-dimensional flow in complex geometry. *J. Comput. Phys.* **62**, 361–382.

Lin, C. C. 1955 *Theory of Hydrodynamic Stability.* Cambridge University Press.

Liu, C. 1997 A numerical investigation of instability and transition in adverse pressure gradient boundary layers. PhD thesis, McGill University.

Mallier, R. 1995 On the onset of three-dimensionality in mixing layers. *Phys. Fluids* A **7**, 1040–1047.

Mallier, R. & Maslowe, S. A. 1994 Fully coupled resonant-triad interactions in a free shear layer. *J. Fluid Mech.* **278**, 101–121.

Mankbadi, R. R., Wu, X. & Lee, S. S. 1993 A critical-layer analysis of the resonant triad in boundary-layer transition: nonlinear interactions. *J. Fluid Mech.* **256**, 85–106.

Mavriplis, C. 1989 Laguerre polynomials for infinite-domain spectral elements. *J. Comput. Phys.* **80**, 480–488.

Nayfeh, A. H. 1987 On subharmonic instability in boundary layers. *ASME Forum on Unsteady Flow Separation.* FED, vol. 52, pp. 37–44.

Obremski, H. J., Morkovin, M. V. & Landahl, M. 1969 A portfolio of stability characteristics of incompressible boundary layers. *AGARDograph* 134. NATO, Paris.

Saric, W. S. & Thomas, A. S. W. 1984 Experiments on the subharmonic route to turbulence in boundary layers. In *Proc. IUTAM Symp. on Turbulence and Chaotic Phenomena in Fluids* (ed. T. Tatsumi), 117–122.

Swinney, H. L. & Gollub, J. P. (Eds.) 1985 *Hydrodynamic Instabilities and the Transition to Turbulence*, 2nd Edn. Springer.

Usher, J. R. & Craik, A. D. D. 1975 Nonlinear wave interactions in shear flows. Part 2. Third-order theory *J. Fluid Mech.* **70**, 437–461.

Williamson, J. H. 1980 Low-storage Runge–Kutta schemes. *J. Comput. Phys.* **35**, 48–56.

Wu, X. 1992 The nonlinear evolution of high-frequency resonant-triad waves in an oscillatory Stokes layer at high Reynolds number. *J. Fluid Mech.* **245**, 553–597.

Zelman, M. B. & Maslennikova, I. I. 1993 Tollmien–Schlichting-wave resonant mechanism for subharmonic-type transition. *J. Fluid Mech.* **252**, 449–478.